

In the previous chapter the analysis procedure and the kinematic fitting technique were introduced (section 5.5 and 5.6). Before the reconstruction of the  $K^0\Sigma^+$  final state we have to analyze the results from the kinematic fit. In this chapter we will discuss the results produced by the kinematic fit. We will also discuss the  $K^0\Sigma^+$  identification, background subtraction and the cross section determination. Furthermore, the experimentally determined cross sections will be compared to predictions from the Isobar Model.

### 6.1 Results from kinematic fit

The measured parameters of all photons and a proton which are given as input to the kinematic fit are modified within the error limits of that parameter. These modified values are checked using a  $\chi^2$  test. The  $\chi^2$  distribution is very important in order to measure the confidence in the results. The smaller the value of  $\chi^2$ , the greater is the confidence in the results.

#### 6.1.1 Confidence Level

If  $\eta_0(\eta_f)$  are the vectors corresponding to initial (final) values of the measured parameters, the  $\chi^2$  value of the fit is given by:

$$\chi^2 = (\eta_0 - \eta_f)^T G_y (\eta_0 - \eta_f) \quad (6.1)$$

where  $G_y$  is the inverse of the covariance matrix. The probability density function  $f(\chi^2)$  of the  $\chi^2$  values for a standard Gaussian distribution (mean = 0,  $\sigma = 1$ ) is given by (equation 6.6.10 in ref. [67]):

$$f(\chi^2) = \frac{1}{\Gamma(\lambda)2^\lambda} (\chi^2)^{\lambda-1} e^{-\frac{1}{2}\chi^2} \quad (6.2)$$

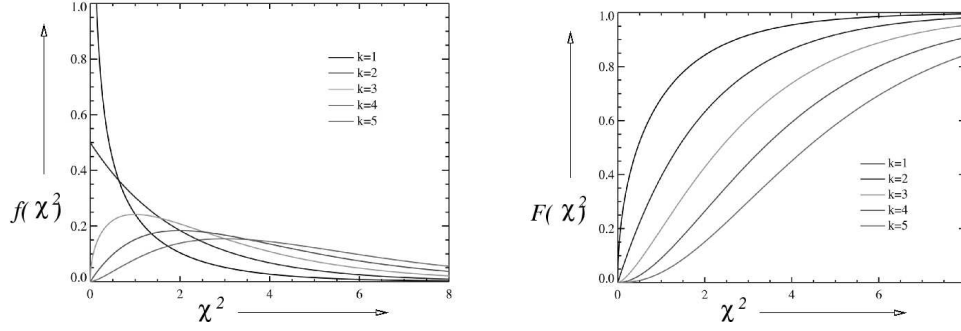


**Figure 6.1:** Left: The probability density of the  $\chi^2$  for a standard Gaussian distribution. Right: The cumulative distribution function for a standard Gaussian distribution as a function of  $\chi^2$ . In this picture the function for  $k=1$  is the curve at the far left and the function for  $k=5$  is at the far right.

where,

$$\lambda = \frac{1}{2}k \quad (6.3)$$

The quantity  $k$  is the number of degrees of freedom. The distribution of  $f(\chi^2)$  is shown in figure 6.1(left). In this picture the probability density distributions are plotted for different number of degrees of freedom. One can see that for  $\chi^2 = 0$ , the probability density diverges for  $k = 1$ , is equal to  $1/2$  for  $k = 2$  and vanishes for  $k \geq 3$ . The cumulative distribution function for  $\chi^2$  gives the probability that the real valued random variable  $u$  is not larger than  $\chi^2$ .

$$F(\chi^2) = \frac{1}{\Gamma(\lambda)2^\lambda} \int_0^{\chi^2} u^{\lambda-1} e^{-\frac{1}{2}u} du \quad (6.4)$$

Such a distribution function for a standard Gaussian distribution is shown in figure 6.1(right). If all measurement errors are properly estimated and no systematic errors are present, then the  $\chi^2$  distribution should follow the distribution as shown in figure 6.1. In practice, one usually uses the quantity:

$$W(\chi^2) = 1 - F(\chi^2) \quad (6.5)$$

which measures the confidence in a measured result.  $W(\chi^2)$  is called the “confidence level”. From this equation 6.5 it follows that the confidence level runs from 0 to 1. A high  $\chi^2$  corresponds to a confidence level close to 0 and a low  $\chi^2$  value corresponds to a confidence level close to 1. If the measured values are

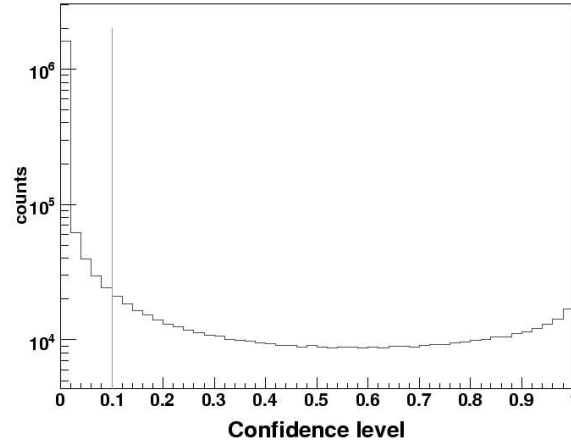


**Figure 6.2:** The confidence level distribution for all fitted events in the experimental data. A cut is placed at 0.10 to select correct events.

distributed according to a Gaussian distribution around the values calculated by the fit, and the measurement errors have been estimated correctly, then the confidence level distribution will be flat.

In figure 6.2 the confidence level for all fitted events in the experimental data is shown. The events which have large  $\chi^2$  value in the fit are located in the peak region close to 0. And the events which have low  $\chi^2$  value are distributed in the region close to 1. The rest of the events is distributed in the flat region. The events with large  $\chi^2$  value are not of interest, because these events most likely do not satisfy the constraint equations. Therefore, in order to get rid of these events, a cut has been placed at 0.1 on the confidence level spectrum, discarding all events with lower confidence level. While the more correct events with low  $\chi^2$  value, which are distributed over the higher confidence levels are kept in the sample.

In figure 6.3 the comparison between the confidence level obtained for the  $K^0\Sigma^+$  channel from the experimental data (solid line) and from the simulated data (dashed line) is shown. The confidence level distribution for the  $\eta$  channel in the experimental data (dotted line) is also shown in the figure. All the distributions are similar which assures consistency in the analysis procedure.

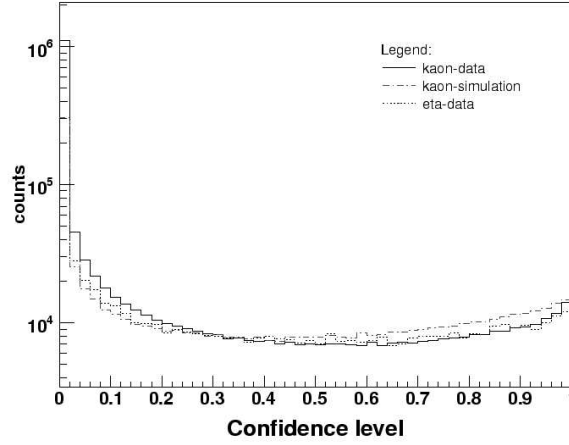


**Figure 6.3:** The confidence levels for data in the  $K^0\Sigma^+$  channel (solid line) and the simulation for the  $K^0\Sigma^+$  channel (dashed line). The confidence level distribution for the  $\eta$  channel in the data is shown by the dotted line. The confidence level distribution for the  $\eta$  channel and that of the  $K^0\Sigma^+$  channel are similar.

### 6.1.2 The Pull distribution

The pull distribution is defined as the difference between measured and final parameters, obtained by the kinematic fit, normalized by the quadratic error difference. If  $\eta_i$  and  $\eta_f$  are elements of the vector of the initial and final values of the measured parameters, respectively, and  $\sigma_i$  and  $\sigma_f$  are the errors on them, then the pull distribution is given by

$$Pull = \frac{\eta_i - \eta_f}{\sqrt{\sigma_{\eta_i}^2 - \sigma_{\eta_f}^2}} \quad (6.6)$$

The pull distribution can provide information about the systematic errors on the measured values. If no such errors exist, the difference between the measured and the fitted values should form a distribution centered at zero. The systematic error will cause a shift in the distribution to either positive or negative values. If the errors on the measured parameters are properly estimated, then, from equation 6.6, the pull distribution should have a mean = 0 and a  $\sigma = 1$ . Figures 6.4 to 6.6 show the pull distributions for  $E, \theta, \phi$ -parameters for photons, proton and incoming photon beam. Figure 6.4 shows the pull distributions for all 6 photons. To obtain these results the confidence-level cut of 10% has been applied. From this figure it can be seen that all distributions are centered around 0 and have

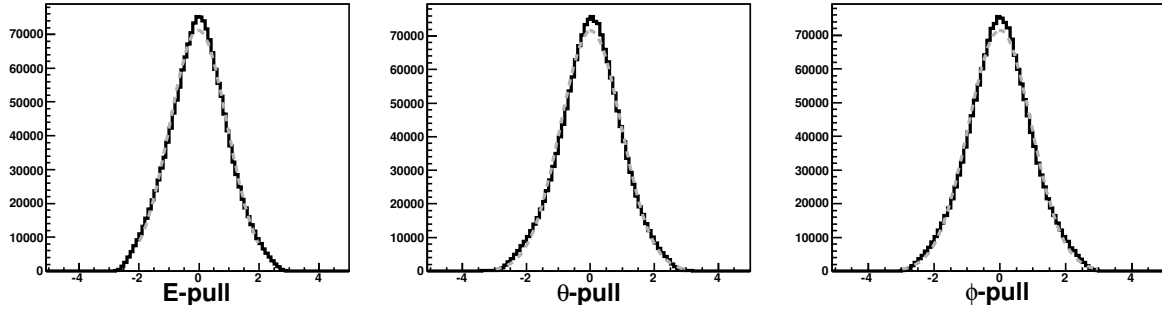


**Figure 6.4:** The  $E, \theta, \phi$ -pull distribution for 6 photons. The gray-dotted line is the fitted Gaussian function with mean = 0 and  $\sigma = 1$ .

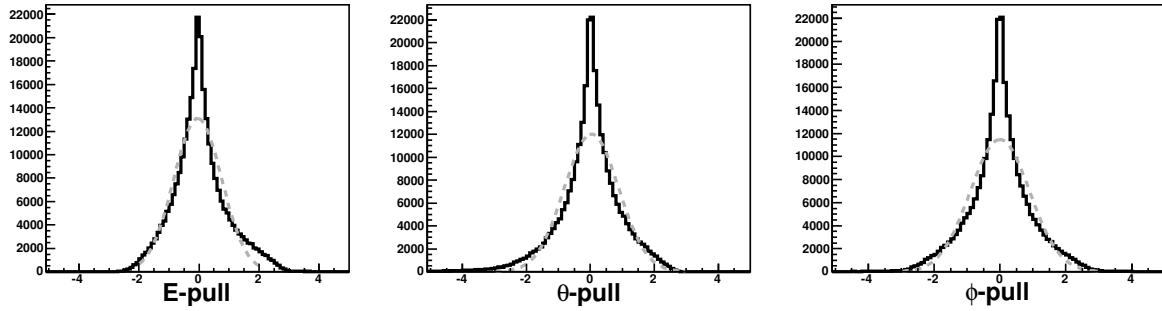


**Figure 6.5:** The  $E, \theta, \phi$ -pull distribution for protons. The gray-dotted line is the fitted Gaussian function.

$\sigma = 1$  for all photons. The  $E, \theta, \phi$ -pull distributions for protons and the photon beam are more narrow than expected for a Gaussian distribution. The reason for this behaviour lies in the fact that the neutron energy and momentum are calculated from the constraint equations.

### 6.1.3 The $\eta$ mass

It is important to make sure that the kinematic fit does not force background events into the signal. This check can be done by using one of the background channels with the same final state as our channel of interest. Since the  $\eta$  production channel has a larger cross section, we used the

$$\gamma d \rightarrow \eta p n \rightarrow \pi^0 \pi^0 \pi^0 p n \rightarrow 6\gamma p n \quad (6.7)$$

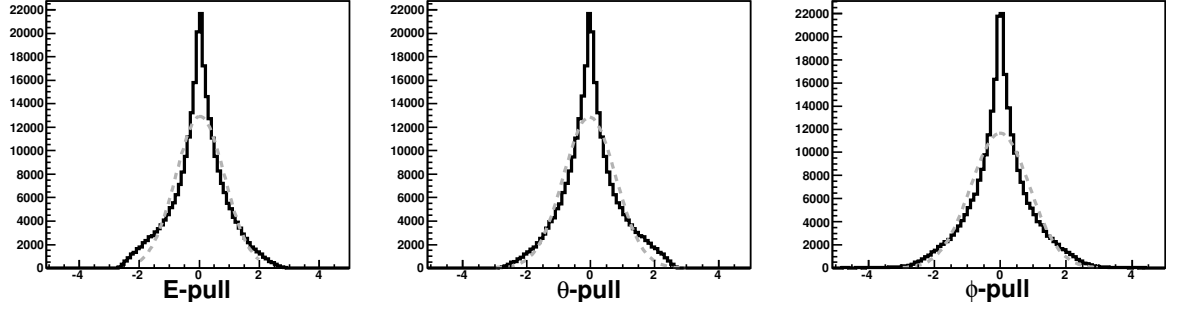


**Figure 6.6:** The  $E, \theta, \phi$ -pull distribution for photon beam. The gray-dotted line is the fitted Gaussian function.

channel to check whether some background events are forced into the  $\eta$  signal. We have produced the  $3\pi^0$  invariant-mass spectrum before and after the kinematic fit. For this purpose a selection of events was made by using a cut on the confidence level spectrum ( $CL \geq 0.1$ ) in order to reject background. These two spectra are shown in figure 6.7. It can be seen that the peak has become much sharper. After the kinematic fit the invariant-mass resolution ( $\sigma$ ) for the  $\eta$  peak improves from 21 MeV to 10 MeV, while the peak content remains the same ( $161439 \pm 401$  before and  $161322 \pm 401$  after the kinematic fit). Also the shape of the background remains as before the kinematic fit. This comparison confirms that the kinematic fit does not force background events into the signal.

## 6.2 Neutron Momentum distribution

In the Monte Carlo simulation (see section 5.3) the neutron momentum was generated according to the Paris model [65]. To check the consistency between the generated and detected neutron, one has to study the correlation between them. However, the neutron momentum measured by the detector setup and the Paris model are not comparable because the experimental resolutions need to be considered. The effect of the experimental resolution was included by adding a Gaussian distribution ( $G$ ) of  $\sigma = 35$  MeV/c to the individual components of the

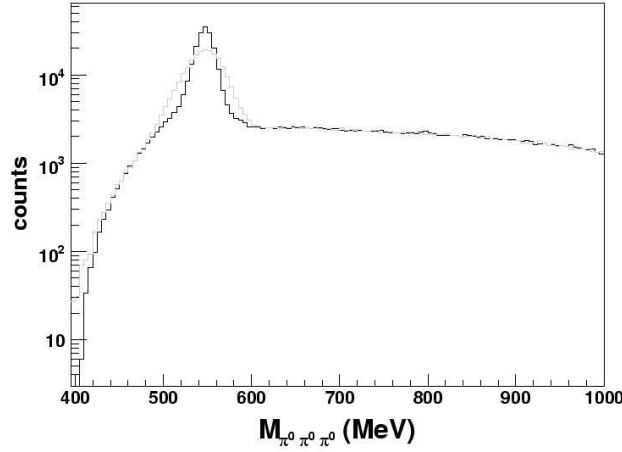


**Figure 6.7:** Comparison of the  $\eta$  peak in the  $3\pi^0$  invariant-mass spectrum after (solid line) and before (dotted line) the kinematic fit. The fit improves the invariant-mass resolution for the  $\eta$  peak, without altering appreciably the background.

generated neutron momentum:

$$\begin{aligned} P'_x &= P_x + G \\ P'_y &= P_y + G \\ P'_z &= P_z + G \end{aligned} \tag{6.8}$$

where  $P_x, P_y, P_z$  are the generated neutron momentum components and  $P'_x, P'_y, P'_z$  are the new components. Then the Paris model including the experimental resolutions provides the momentum:

$$|\vec{P}_{n,Res}| = \sqrt{(P'_x)^2 + (P'_y)^2 + (P'_z)^2} \tag{6.9}$$

For the study in this thesis  $|\vec{P}_n|$  is reconstructed from energy and momentum constraint equations in the kinematic fit (see equation 5.17). The kinematic fit gives the value of the neutron four-momentum  $(P_x, P_y, P_z, E)$ . The reconstructed value of the neutron momentum for the Monte Carlo simulated data (section 5.3) is determined by:

$$|\vec{P}_{n,Sim}| = \sqrt{(P_{x,Sim})^2 + (P_{y,Sim})^2 + (P_{z,Sim})^2} \tag{6.10}$$

Similarly, for the experimental data the neutron momentum is reconstructed

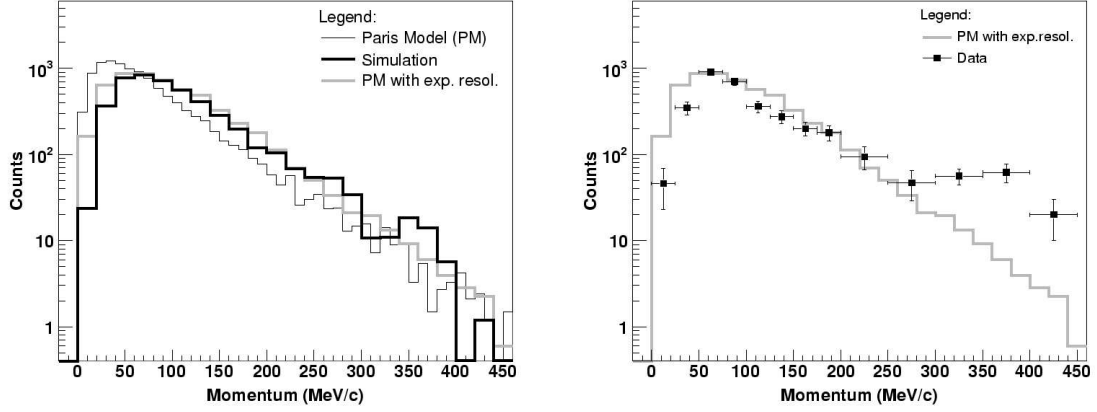


**Figure 6.8:** The neutron momentum distribution. Left: the comparison of the neutron momentum distribution for the Paris model (thin solid line), the Paris model including experimental resolutions (equation 6.9) (gray line) and the calculated neutron momentum in the Monte Carlo simulation (equation 6.10) (black line). Right: the Paris model including experimental resolutions is compared with the neutron momentum in the experimental data (equation 6.11).

using:

$$|\vec{P}_{n,Data}| = \sqrt{(P_{x,Data})^2 + (P_{y,Data})^2 + (P_{z,Data})^2} \quad (6.11)$$

The comparison between the neutron momentum from the Paris model and results from equation 6.9 and equation 6.10 is given in figure 6.8 (left). The Paris model is indicated by the thin solid line. When the experimental resolutions are included (equation 6.9), the distribution from the Paris model becomes broader and shifted to the high-energy side (shown by the gray line in figure 6.8 (left)). The calculated neutron momentum for the simulated data (equation 6.10) is shown by the thick solid line. A reasonable agreement between the Paris model including the experimental resolution and the reconstructed neutron momentum in the simulation can be seen.

The comparison of the neutron momentum distribution for the experimental data and the simulation is shown in figure 6.8 (right). In this graph the Paris model including the experimental resolutions is shown by the gray line. The squares are the data points obtained from this experiment. A good agreement between simulation and data points can be seen up to  $|\vec{P}_n| = 200$  MeV/c. For  $|\vec{P}_n| > 200$  MeV/c a tail structure appears in the data which does not agree



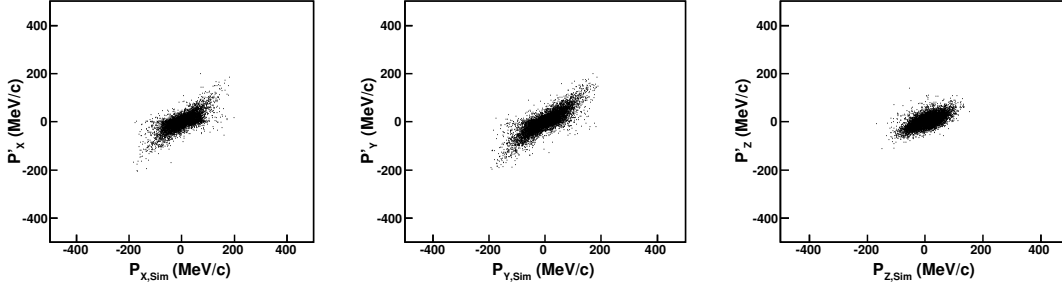


**Figure 6.9:** The neutron momentum correlation for  $|\vec{P}_n| \leq 200$  MeV/c. The reconstructed momentum in the simulation vs neutron momentum by the Paris model including resolution is plotted for individual neutron momentum components.

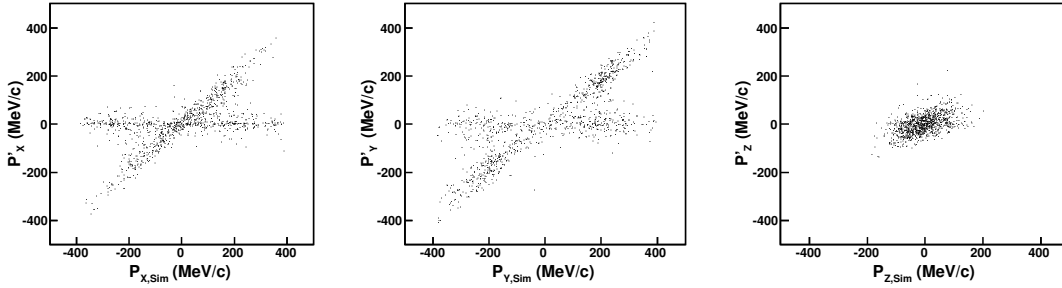


**Figure 6.10:** The neutron momentum correlation for  $|\vec{P}_n| > 200$  MeV/c. The reconstructed momentum in the simulation vs neutron momentum by the Paris model including resolution is plotted for individual neutron momentum components.

with the simulation. In a detailed study we investigated the individual neutron momentum components.

The correlation between the reconstructed neutron momentum in the simulation and the neutron momentum obtained by the Paris model including the experimental resolutions is shown in figure 6.9. The events shown in these graphs are selected for  $|\vec{P}_n| \leq 200$  MeV/c. A neutron momentum resolution  $\sigma_{P_x} = \sigma_{P_y} = \sigma_{P_z} = 30$  MeV/c has been determined. The equivalent picture for  $|\vec{P}_n| > 200$  MeV/c is depicted in figure 6.10. It is observed that here the correlation for  $P_x, P_y, P_z$  is overlaid by a strong background contribution. The kinematic fit routine failed to reconstruct the neutron momentum for these events. These events are not reliable for further analysis. Therefore we decided to analyze only events with  $|\vec{P}_n| \leq 200$  MeV/c, allowing about 85% of the total number of events.

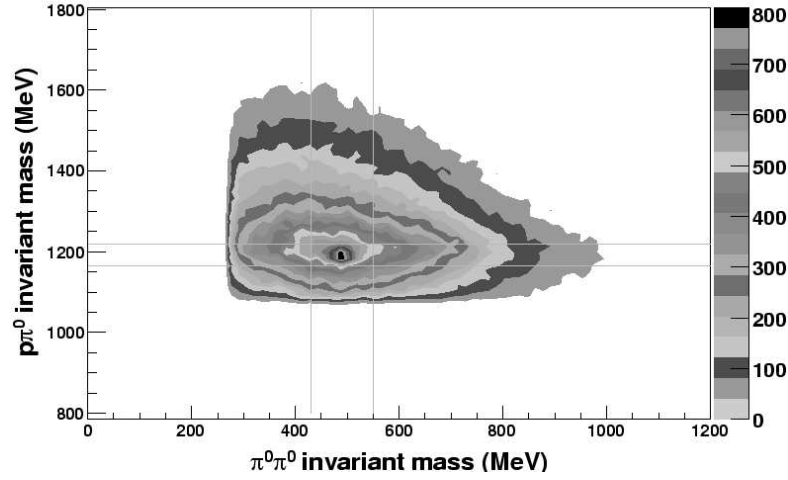


**Figure 6.11:** The distribution of the  $\pi^0\pi^0$  invariant mass in dependence of the  $p\pi^0$  invariant mass after the kinematical fit with a cut on confidence level ( $CL \geq 0.10$ ).

### 6.3 $K^0$ and $\Sigma^+$ identification

After the kinematic fit and the selections described in the earlier sections only events containing  $3\pi^0$ 's are left in the data. To extract the  $K^0\Sigma^+$  signal from the kinematically fitted data the background needs to be removed as much as possible. This is explained in the following sections.

#### 6.3.1 Removing the $\eta \rightarrow 3\pi^0$ channel

As the largest (see figure 6.7) contribution to the events containing  $3\pi^0$ 's results from  $\eta$  photoproduction, we have to remove these events from the data. This is accomplished by removing all events with the  $\pi^0\pi^0\pi^0$  invariant mass in the range 510 – 580 MeV. The events surviving this cut are passed on to further analysis.

#### 6.3.2 Extracting the $K^0$ and $\Sigma^+$ signal

In the next step the three  $\pi^0$ 's and the proton are combined into a  $K^0\Sigma^+$  pair, which can be done in three different combinations. For all three combinations the  $\pi^0\pi^0$  invariant-mass is analyzed as a function of the  $\pi^0p$  invariant mass, as shown in figure 6.11. To select the  $K^0$  signal a window has been placed around the  $\Sigma^+$  mass and the selected events are projected on the x-axis. Similarly, to select the  $\Sigma^+$  signal a window has been placed around the  $K^0$  mass and the

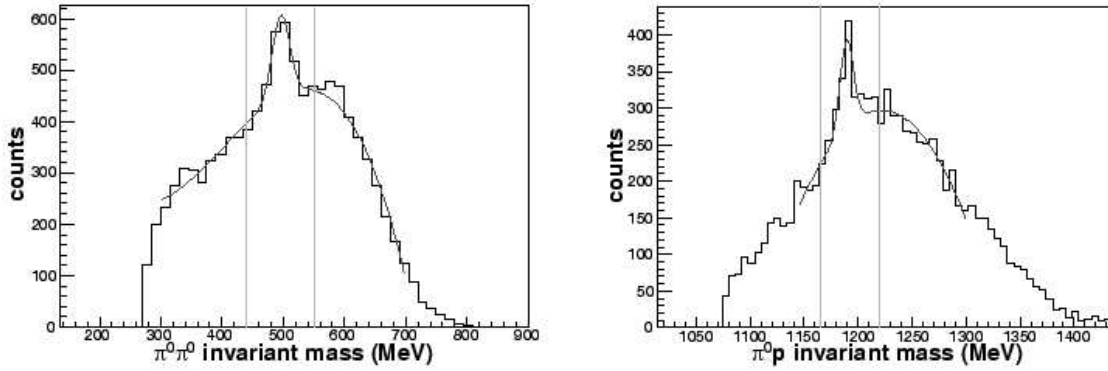


**Figure 6.12:**  $\pi^0\pi^0$  invariant mass and  $\pi^0p$  invariant mass after a cut on confidence level ( $CL \geq 0.10$ ). A peak at the  $K^0$  mass (left picture) and the  $\Sigma^+$  mass (right picture) can be seen. In both pictures the signal is fitted by the function which is composed of a Gaussian distribution and a polynomial.

events are projected. The projected signals are shown in figure 6.12. The peaks at the  $K^0$  and  $\Sigma^+$  mass can be seen along with the background. The lines shown in the picture are the windows used to make the projection for the  $K^0$  and  $\Sigma^+$  signals respectively. Corresponding lines are also shown in figure 6.11. In both pictures the signals are fitted by a Gaussian function and the background is fitted by a polynomial.

### 6.3.3 Remaining background subtraction

After the cut on  $\eta$  invariant mass and using  $K^0$  and  $\Sigma^+$  mass windows (as explained in the previous section), still a considerable background remains below the signal. The simulation shows that combinatorial background (events in which the wrong combination of photons was chosen to form a  $\pi^0$ ) is negligible. The main source of this background is caused by sequential decay of resonances, where a high-lying resonance is created, which decays into a lower-lying resonance through  $\pi^0$  emission, which in turn decays in the same way to the next resonance until  $3\pi^0$ 's, a proton and a neutron are left. As the reaction:

$$\gamma d \rightarrow \pi^0\pi^0\pi^0pn \rightarrow 6\gamma pn \quad (6.12)$$

results in the same final state as the channel of interest, it will contribute to the background. This background is parametrized and subsequently subtracted as a polynomial function from the  $\pi^0\pi^0$  invariant-mass spectrum which is obtained

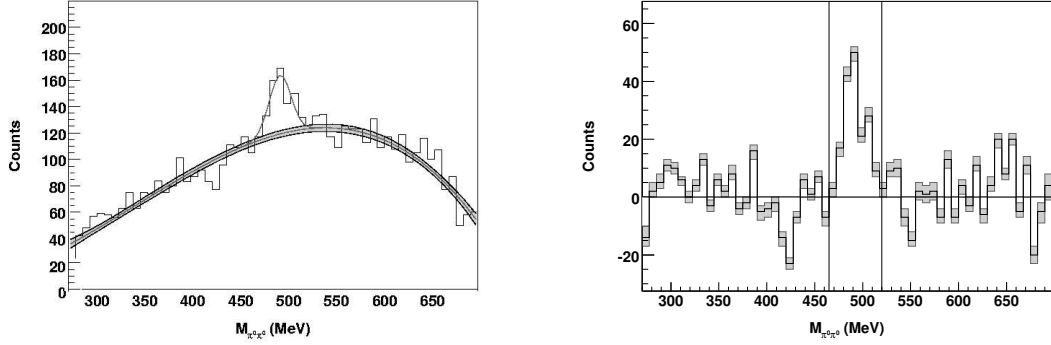


**Figure 6.13:** Left: an example of a  $K^0$  invariant-mass spectrum ( $1350 \text{ MeV} \leq E_{\text{tagger}} \leq 1450 \text{ MeV}$ ) is shown, together with the background fit. Right: the same spectrum is shown after the background subtraction. The gray rectangles in this plot show the uncertainty in the background subtracted signal due to the uncertainty in the background fit. The  $K^0$  mass resolution ( $\sigma$ ) of 12 MeV has been observed.

after a cut on the  $\Sigma^+$  mass. In such a spectrum, the  $K^0$  signal is fitted by a Gaussian function and the shape of the background is determined by fitting a 3rd order polynomial function outside the  $K^0$  peak region (see figure 6.13(left)). The fitted polynomial function has the form

$$y = a + bx + cx^2 + dx^3 \quad (6.13)$$

where  $a, b, c$  and  $d$  are the constants determined by the fit. The thick band shown in the picture is the uncertainty in the fit. Then the fitted polynomial function is subtracted from the  $\pi^0\pi^0$  invariant-mass spectrum. This gives the background-subtracted  $K^0$  signal. The resulting spectrum is then integrated over the region of  $3\sigma$  around the peak as shown in figure 6.13(right). The bin size chosen for the extraction of the signals is 100 MeV in incoming photon beam energy as determined by the measured tagger energy.

The  $K^0\Sigma^+$  production on the free proton target has been studied recently ([15]) using the same experimental setup explained in this thesis. The  $\pi^0\pi^0$  invariant-mass spectrum obtained on the free proton target is shown in figure 6.14. This graph was generated after the gate on the  $\Sigma^+$  mass on the  $\pi^0p$  mass spectrum. The background contribution shown in this spectrum is stemming from only sequential  $3\pi^0$  decay. The comparison of figure 6.13 and figure 6.14 shows that the background contribution from the sequential  $3\pi^0$  decay process

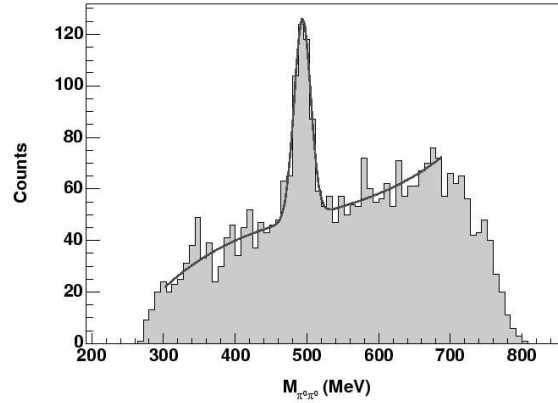


**Figure 6.14:** The  $\pi^0\pi^0$  invariant-mass spectrum obtained from the free proton target (taken from [15]) after the kinematic fit and gated on the  $\Sigma^+$  mass. In this graph the line shows the combined fit of the background and the  $K^0$  signal. The  $K^0$  mass resolution ( $\sigma$ ) of 10 MeV has been observed.

on the deuteron target is three times higher than that measured on the free proton target. The  $K^0$  photoproduction cross section on the deuteron target is about 45% lower (figure 6.27).

## 6.4 Acceptance determination

The  $K^0\Sigma^+$  acceptance was determined from the Monte Carlo simulation of the experimental set up using Geant. The  $K^0\Sigma^+$  events were generated and treated in exactly the same manner as in the experimental data. The acceptance is determined by the number of reconstructed events divided by the number of generated events. To attain consistency in the analysis of experimental and simulated data, the same energy calibration procedures were used to analyze simulated data as experimental data, and one analysis program was used to analyze both data sets. In addition, trigger conditions (see section 3.3) responsible for selecting the data on-line were also applied to the simulated data. The acceptance as function of incoming photon beam energy is shown in figure 6.15. The bin width in beam energy was chosen to be 100 MeV. The acceptance is flat and almost constant over the beam energy region except for the first energy point near the production threshold. The  $K^0$  acceptance as a function of the center-

Selection	Acceptance
Total no. of events generated	100%
No. of events with 7 hits	48.2%
No. of events with 6 photons and 1 proton	33.27%
Taps - Tagger coincidence	94.29%
Fitted events	87.12%
$K^0\Sigma^+$ reconstructed events	57.63%

**Table 6.1:** Summary of the acceptance determination. The first column explains the selection applied to the simulated data. The numbers in the second column indicate the percentage of events surviving after the selection has been applied.

of-mass  $K^0$  angle is shown in figure 6.16. Table 6.1 shows the summary of the acceptance determination.

## 6.5 Cross section

The cross sections were determined using the equation:

$$\sigma_{tot}(E_\gamma) = \frac{N_{events}(E_\gamma)}{acc(E_\gamma) \cdot \xi \cdot N_\gamma(E_\gamma) \cdot \Gamma_{br}} \quad (6.14)$$

where,

$N_{events}(E_\gamma)$  is the total number of  $K^0\Sigma^+$  events in the measured data for a particular photon beam-energy window,  $acc(E_\gamma)$  is the acceptance for this channel in that photon beam-energy window (determined from the simulation),  $\xi$  is the target density,  $N_\gamma(E_\gamma)$  is the total number of tagged photons in the photon beam-energy window,  $\Gamma_{br}$  is the branching ratio for this reaction channel.

The target density is calculated using the formula:

$$\xi = \frac{N_{av} \cdot \rho \cdot L}{A} \quad (6.15)$$

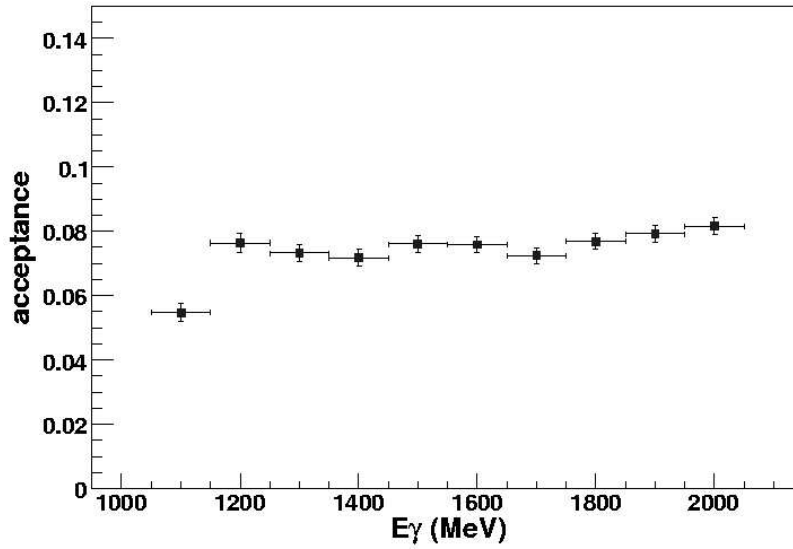


Figure 6.15: The  $K^0\Sigma^+$  acceptance as a function of incoming photon beam energy.

where,

$N_{av} = 6.022 \cdot 10^{23} \text{ mol}^{-1}$ ,  $\rho$  = density of the liquid deuterium target =  $0.169 \text{ g/cm}^3$ ,  $L$  = length of the target =  $5 \text{ cm}$ ,  $A$  = atomic weight =  $2.0140$ . Using these values, the target density is found to be  $\xi = 2.5266 \cdot 10^{23} \text{ cm}^{-2}$ .

The branching ratio for the process

$$\gamma d \rightarrow K^0\Sigma^+ n \rightarrow \pi^0\pi^0\pi^0 pn \rightarrow 6\gamma pn \quad (6.16)$$

is 7.8%. The number of incoming photons passing through the target are estimated by using the procedure explained in section 5.7. The total cross section is determined for an incoming photon beam-energy window of 100 MeV. The total cross section as a function of beam energy is shown in figure 6.17.

The differential cross sections as a function of the  $K^0$  angle and the  $\Sigma^+$  angle  $\theta'_{\Sigma^+}$  (ref. figure 2.7) obtained from this work are shown in figure 6.18 and 6.19, respectively.

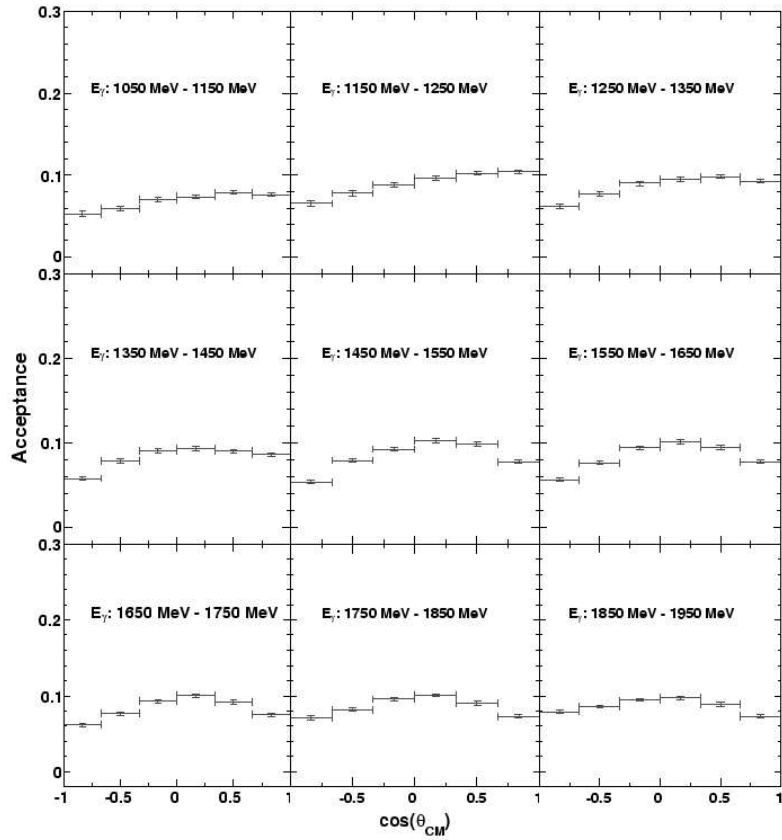


**Figure 6.16:** The acceptance as a function of the cosine of the kaon center-of-mass angle. The acceptances are plotted from threshold (1050 MeV) upto 1950 MeV in steps of 100 MeV. It can be seen that the acceptances are at the same level for all energy windows.



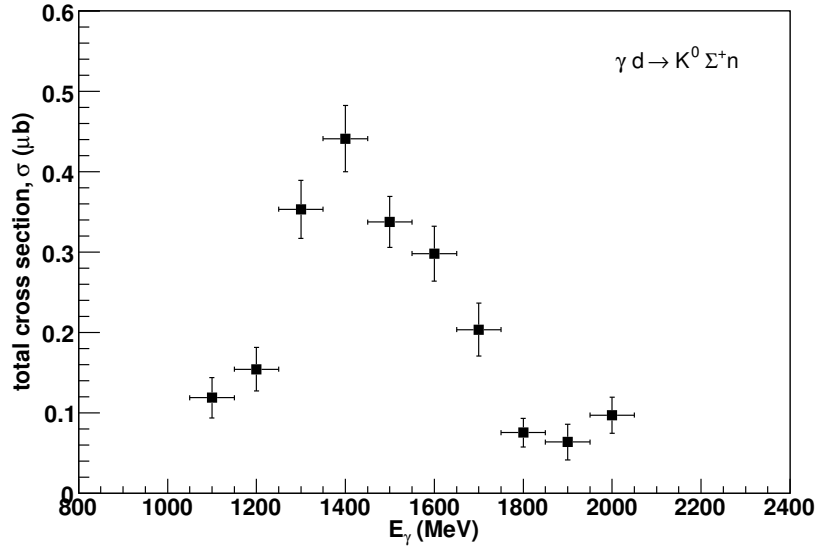


**Figure 6.17:** The total cross section for  $K^0$  photo-production as a function of incoming photon beam energy.

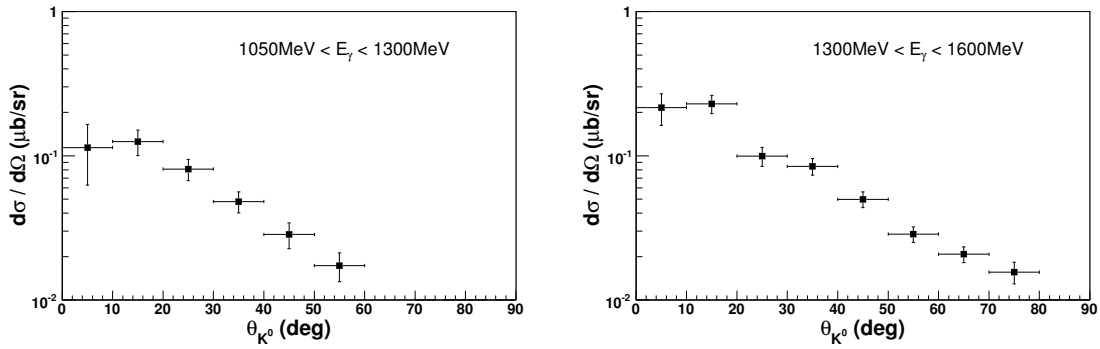


**Figure 6.18:** The  $K^0$  differential cross section as a function of  $K^0$  angle (lab) obtained in this work. The cross sections are plotted for two photon beam-energy windows  $1050 \text{ MeV} < E_\gamma < 1300 \text{ MeV}$  and  $1300 \text{ MeV} < E_\gamma < 1600 \text{ MeV}$ .

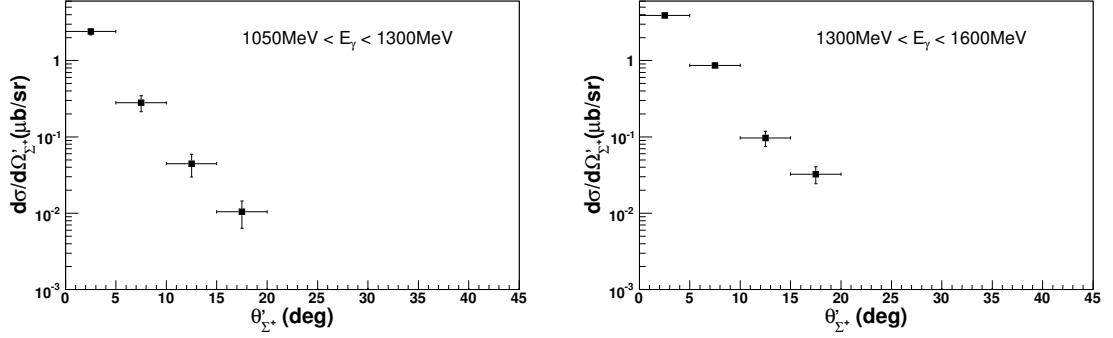


**Figure 6.19:** The  $K^0$  differential cross section as a function of  $\Sigma^+$  angle (lab) obtained in this work. In this picture the hyperon angle ( $\theta_{\Sigma^+}^l$ ) with respect to momentum transfer in the  $\Sigma^+n$  system is shown (for definition of  $\theta_{\Sigma^+}^l$  ref. figure 2.7). The cross sections are plotted for two photon beam energy windows  $1050 \text{ MeV} < E_\gamma < 1300 \text{ MeV}$  and  $1300 \text{ MeV} < E_\gamma < 1600 \text{ MeV}$ .

## 6.6 Statistical error

The statistical uncertainty in the number of  $K^0$  counts is determined by:

$$\frac{\Delta S}{S} = \frac{\sqrt{S+B}}{S} \quad (6.17)$$

where,  $S$  is the number of counts in the peak, and  $B$  the number of counts in the background. This equation does not take into account the uncertainty in the fitted background. The error in the background fit also contributes to the total error. This error is determined using the covariance matrix, which is obtained from the fit. Figure 6.13 right (in the manuscript) shows the uncertainty in the background fit as gray bands. The final statistical error is then obtained by adding quadratically the two relative errors.

## 6.7 $\Sigma^+ - n$ relative momentum difference

The relative momentum difference  $|\vec{k}|$  in the  $\Sigma^+n$  system ( $|\vec{k}| = |\vec{P}_{\Sigma^+} - \vec{P}_n|$ ) is a very important parameter to study the final-state interaction. In order to form a  $\Sigma^+n$  bound system, both particles should carry similar momentum. Figure 6.20 shows the kaon momentum  $P_{K^0}$  plotted as a function of  $|\vec{k}|$  for incoming photon beam-energies  $E_\gamma = 1.1 \text{ GeV}$ ,  $1.5 \text{ GeV}$  and  $2 \text{ GeV}$  with  $100 \text{ MeV}$  wide windows

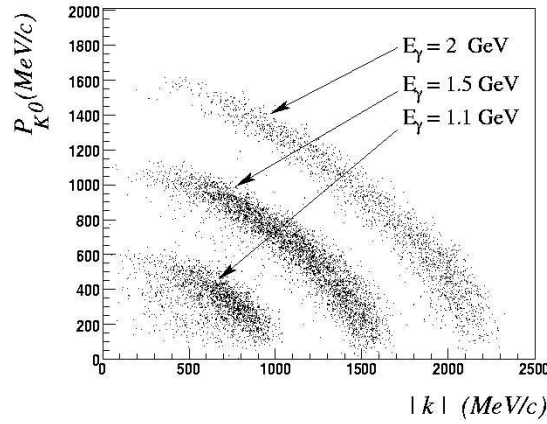


**Figure 6.20:** The kinematical distribution of kaon momentum as a function of the relative momentum,  $|\vec{k}|$ , at a photon beam energy of 1.1 GeV, 1.5 GeV and 2 GeV. The maximum kaon momentum at particular photon beam energy corresponds to forward going kaons. This region can be seen at low relative momentum. In other words, at lower  $|\vec{k}|$  the kaons have highest momentum at particular energy and go into forward direction.

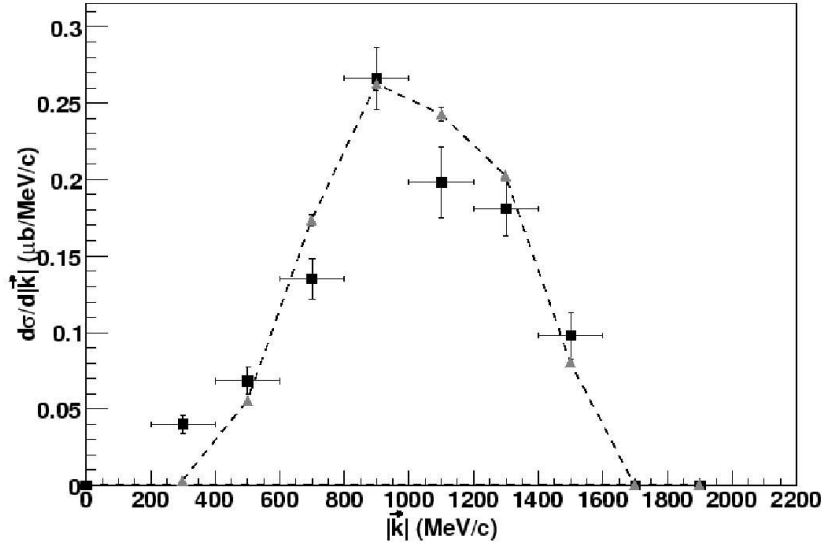


**Figure 6.21:** Differential cross section as a function of the relative momentum difference ( $|\vec{k}| = |\vec{P}_{\Sigma^+} - \vec{P}_n|$ ) for  $1050 \text{ MeV} < E_\gamma < 1600 \text{ MeV}$ . The squares are the data points obtained from this experiment and the dashed line is the Monte Carlo simulation normalized by one common factor to the data point with highest cross section.

at each energy. The bands in the picture show the kinematical correlation. It can be seen that at the higher beam-energy also the higher maximum  $K^0$  momentum is reached. The maximum of the  $K^0$  momentum is reached at  $\theta_{K^0} = 0^\circ$ , where also the maximum final-state effect is expected.

In figure 6.21, the differential cross section is plotted as a function of  $|\vec{k}|$ . The cross section shows a peak around  $|\vec{k}| = 900$  MeV/c and drops towards lower  $|\vec{k}|$ . The maximum value of  $|\vec{k}|$  is limited to 1600 MeV/c. This is because of the condition  $1050 \text{ MeV} < E_\gamma < 1600 \text{ MeV}$  used while plotting this picture. In figure 6.21 the data points are compared to the Monte Carlo simulation. The phase space simulation reproduces the shape of the  $|\vec{k}|$  distribution. The data point for  $|\vec{k}| < 500$  MeV/c lies significantly above the simulation. This difference at the smallest measurable relative momentum might be caused by the  $\Sigma^+n$  FSI effect which is not present in the simulation. In calculations by A. Salam [23] it is predicted that the FSI effect is prominent for higher hyperon angles. Therefore an attempt has been made to produce hyperon angular distributions for lower and higher  $|\vec{k}|$  values. In figure 6.22 (left) the differential cross section for the  $\Sigma^+$  angle (lab) has been plotted for  $|\vec{k}| \leq 500$  MeV and  $|\vec{k}| > 500$  MeV. The suppression in the cross section values for lower values of  $|\vec{k}|$  is due to phase space limitations. However, there is also a considerable difference in the shape of both curves. In fact, this change is very prominent at higher  $\Sigma^+$  angles. In the right-side of figure 6.22, the ratio of  $\Sigma^+$  angular distributions for  $|\vec{k}| \leq 500$  MeV/c to  $|\vec{k}| > 500$  MeV/c is plotted. The ratio in the phase space simulation is indicated by the inverted triangles. It shows that the ratio rises towards larger hyperon angles for the experimental data, however, for the phase space simulation it remains at the same level. This effect might be related to the  $\Sigma^+n$  final-state interaction.

## 6.8 Comparison to theory

The calculations for  $K^0$  photoproduction on the deuteron were performed by A. Salam [42] using the Isobar Model (described in section 2.5). In figure 6.23, the excitation function is compared to these calculations. The calculations are done for the  $\gamma d \rightarrow K^0 \Sigma^+ n$  channel for impulse approximation (IA) and IA including  $YN$  rescattering effects. The calculated cross section predicts that the effect due to  $YN$  rescattering is negligible for this observable. The coupling constants in the Isobar Model calculations were fitted to the kaon photoproduction on the

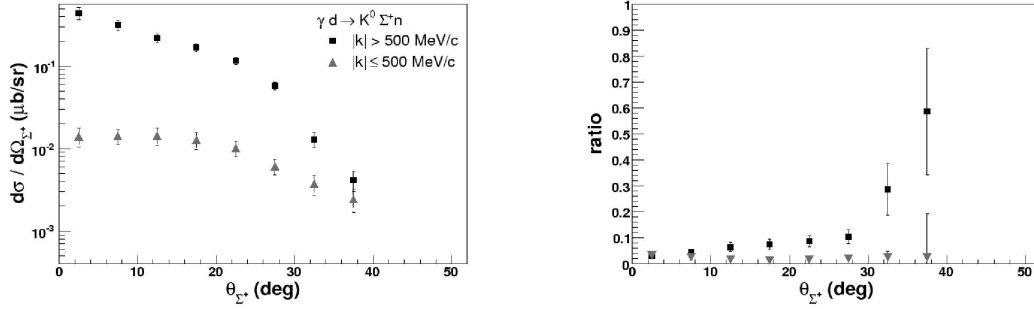


**Figure 6.22:** Left side: differential cross section as a function of the  $\Sigma^+$  angle. The squares are for the condition that  $|\vec{k}| > 500 \text{ MeV/c}$  and the triangles are for  $|\vec{k}| \leq 500 \text{ MeV/c}$ . The two distributions do not have the same shape. This effect might be due to the final-state  $\Sigma^+n$  interaction. Right side: the ratio between the two distributions shown in the left-side as a function of the  $\Sigma^+$  angle. The ratio obtained from the data points (squares) is compared with the ratio in phase space simulation (inverted triangles).

proton target ( $\gamma p \rightarrow K^+\Lambda$ ,  $\gamma p \rightarrow K^+\Sigma^0$  and  $\gamma p \rightarrow K^0\Sigma^+$  [12, 13]) as measured by the SAPHIR collaboration. The comparison with data points shows that the peak in the predicted cross section is too high. Since no data at all are available in the neutron channel, the corresponding coupling constants were adjusted.

The differential cross sections as a function of kaon angle for the experimental data are compared with the calculations in figure 6.24. In this graph the calculations are shown for the impulse approximation (IA) only and IA including  $YN$  rescattering. According to these calculations the  $YN$  rescattering effect is negligible for this observable, too. The experimental data, however, show strong disagreement with the calculations. The predicted cross sections are different not only in terms of absolute value but also in terms of shape. The data show a tail-like structure and the calculations are steeper towards the higher  $K^0$  angles. This might be interpreted as clear evidence for the fact that 2-step processes play a strong role for this observable. The published calculations by A. Salam [23] show remarkable effects in the  $K^0$  angular distribution due to the  $\pi K$ -process at larger angles (figure 2.6 (right)).

The differential cross section as a function of hyperon angle ( $\theta'_{\Sigma^+}$ ) for the experimental data is compared to the calculations in figure 6.25. The calculations are performed for  $E_\gamma = 1300 \text{ MeV}$ ,  $\theta_{K^0} = 10^\circ$  and  $p_{K^0} = 750 \text{ MeV/c}$ . The data points are plotted for  $1250 \text{ MeV} < E_\gamma < 1350 \text{ MeV}$ ,  $0^\circ < \theta_{K^0} < 20^\circ$  and  $700 \text{ MeV/c} < p_{K^0} < 800 \text{ MeV/c}$ . The calculations are lower than the measured

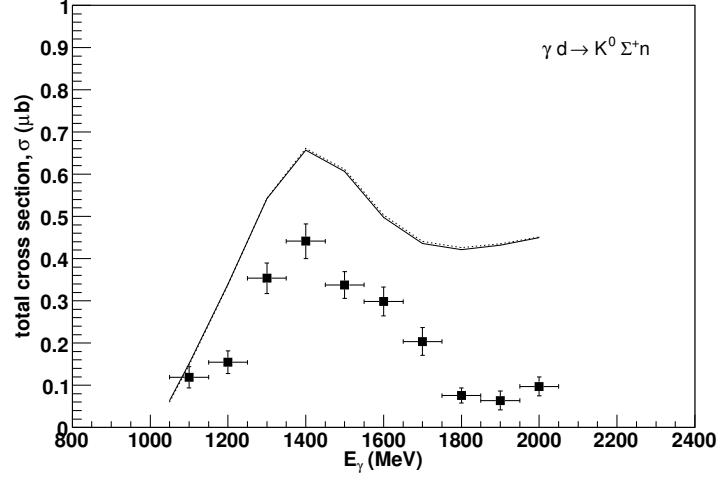


**Figure 6.23:** The excitation function for  $K^0\Sigma^+$  photoproduction as a function of photon beam energy, compared to the predictions by A. Salam [42]. The impulse approximation is shown by the dotted line. When the term for  $YN$  rescattering (solid line) is included, the effect on the total cross section is negligible (these curves are lying on top of each other).

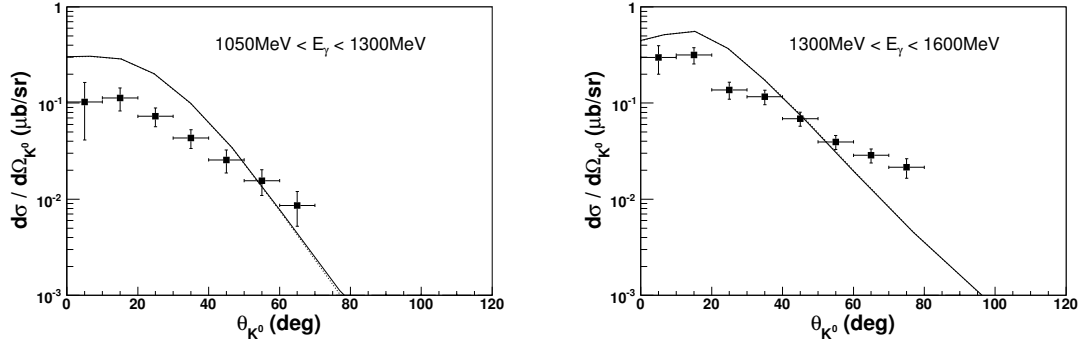


**Figure 6.24:** The differential cross section as a function of kaon angle. The data points are compared with calculations by A. Salam[42]. In this observable the effects due to  $YN$  rescattering (solid line) are negligible. The data points and the calculations show disagreement. Not only the absolute values are different but also the shape of the distribution is different.

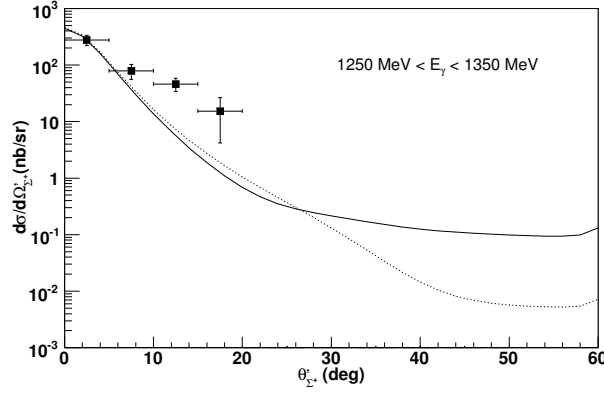


**Figure 6.25:** The differential cross section as a function of hyperon angle  $\theta_{\Sigma^+}'$  is compared with the calculations. The calculations for impulse approximation (IA) (dotted line) and IA including  $YN$  rescattering (solid line) are shown for  $E_\gamma = 1300$  MeV,  $\theta_{K^0} = 10^\circ$  and  $p_{K^0} = 750$  MeV/c. The data points are plotted for  $1250 \text{ MeV} < E_\gamma < 1350 \text{ MeV}$ ,  $0^\circ < \theta_{K^0} < 20^\circ$  and  $700 \text{ MeV/c} < p_{K^0} < 800 \text{ MeV/c}$ . The predicted calculations are lower than the measurements. In this graph the calculations are normalized to the data with highest cross section to compare the shape of the distribution (for details see text).

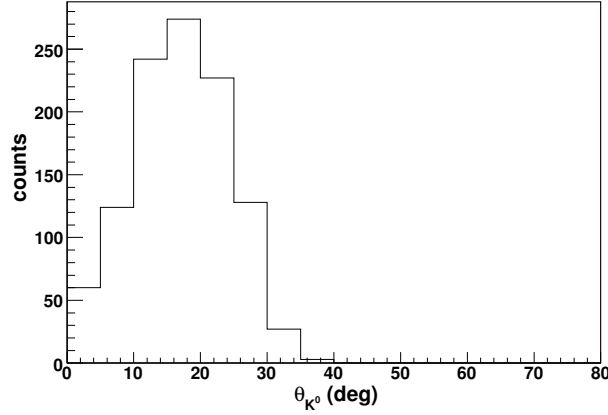


**Figure 6.26:** The  $K^0$  angular distribution in the phase space simulation for photon beam energy  $1250 \text{ MeV} < E_\gamma < 1350 \text{ MeV}$  and kaon momentum  $700 \text{ MeV/c} < p_{K^0} < 800 \text{ MeV/c}$ .

data points by about a factor 3 for this kinematics. This discrepancy might be caused by a too large bin widths, which was chosen to achieve sufficient statistical accuracy. Particularly the phase space simulation (figure 6.26) for the  $K^0$  angular distribution for  $1250 \text{ MeV} < E_\gamma < 1350 \text{ MeV}$  and  $700 \text{ MeV/c} < p_{K^0} < 800 \text{ MeV/c}$  reveals that the cross section depends strongly on the kaon angle. Therefore, to compare the data and calculations for a range of hyperon angles, an accurate integration over the bin widths is required in the calculations. In figure 6.25 the calculations are normalized to the data point with highest cross section by a common factor. Furthermore, the calculations predict that the  $YN$  rescattering effect is rather small and can only be observed at larger hyperon angles. The experimental data is limited to  $\theta'_{\Sigma^+} \leq 20^\circ$ , therefore, this effect can not be seen in our data set.

## 6.9 Comparison to the proton data

The  $K^0$  photoproduction on the free proton target has been extensively studied by R. Castelijns (CBELSA/TAPS collaboration)[15], SAPHIR [12] and CLAS [14] collaboration in  $\gamma p \rightarrow K^0 \Sigma^+$  reaction. The SAPHIR and CLAS collaboration has measured the reaction using the following decay channels :

$$\begin{aligned}\gamma p &\rightarrow K^0 \Sigma^+ \rightarrow (\pi^+ \pi^-)(n \pi^+) \\ \gamma p &\rightarrow K^0 \Sigma^+ \rightarrow (\pi^+ \pi^-)(p \pi^0)\end{aligned}\tag{6.18}$$

and Castelijns has measured the

$$\gamma p \rightarrow K^0 \Sigma^+ \rightarrow (\pi^0 \pi^0)(\pi^0 p) \rightarrow 6\gamma p\tag{6.19}$$

channel. In a full coupled-channel K-matrix calculation Usov and Scholten [16] achieve good agreement with the CBELSA/TAPS data by including a  $P_{13}(1830)$  resonance in their calculations.

The comparison of the  $K^0$  photoproduction for the experimental data and the Isobar Model calculations for the free proton target and the deuteron target are shown in figure 6.27. The Isobar Model (gray curve in the figure) was fitted to the latest SAPHIR data. The CBELSA/TAPS data on the  $K^0$  photoproduction off the free proton [15] (indicated by the gray squares) show a disagreement with the calculations. The calculations are overestimating the measurements. The Isobar Model prediction for  $K^0$  photoproduction off the deuteron is shown



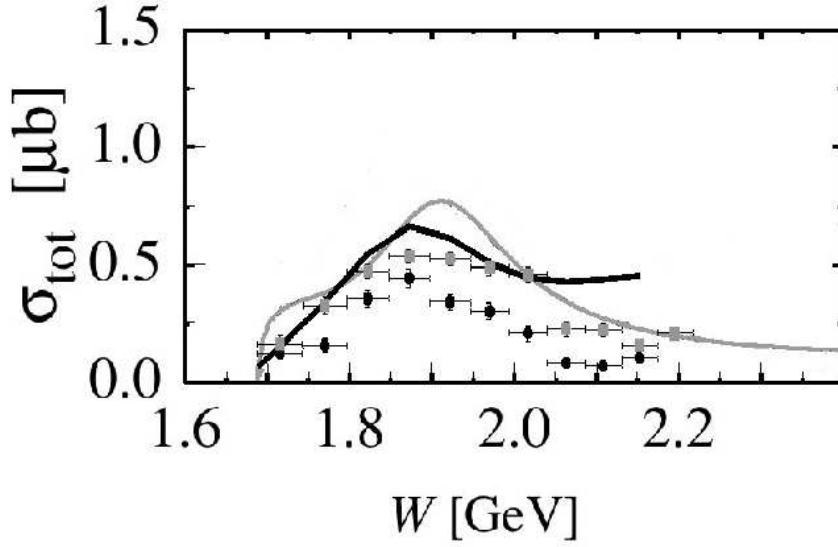


**Figure 6.27:** The total cross section obtained from this work is compared with the total cross section on the free proton. The calculations on proton and deuteron use the Isobar Model as a function of center-of-mass energy  $W$ . In this figure, the gray line is the Isobar Model calculation [44] fitted to the SAPHIR data. The gray squares are the CBELSA/TAPS data on the free proton target [15]. The Isobar Model prediction for the deuteron target [42] is shown by the black line and the data points obtained from this work are shown by the black circles.

by the black line and the data obtained from this thesis work are indicated by the black circles. This comparison also shows the disagreement between the predictions and the data points for the deuteron target. The predicted cross sections for the deuteron are lower than the calculations for the free proton. The same behaviour can be seen for the experimental data, too. The data points for the deuteron target are lower than those for the free proton target. New calculations on the deuteron target are recommended. By fitting the coupling constants to the CBELSA/TAPS data one may achieve a consistent description of the photoproduction from the proton and deuteron targets.

